The Astronomical Journal, 153:32 (12pp), 2017 January doi:10.3847/1538-3881/153/1/32

A NEW LOOK AT THE INTEGRATED RADIO/MICROWAVE CONTINUUM SPECTRUM OF GALACTIC SUPERNOVA REMNANT IC 443

D. Onić[1], D. Urošević[1,2], and D. Leahy[3]
[1] Department of Astronomy, Faculty of Mathematics, University of Belgrade, Serbia; donic@matf.bg.ac.rs
[2] Isaac Newton Institute of Chile, Yugoslavia Branch
[3] Department of Physics and Astronomy, The University of Calgary, Canada
Received 2016 July 18; revised 2016 November 15; accepted 2016 November 25; published 2016 December 29

ABSTRACT

Recent observations of the microwave sky, by space telescopes such as the *Wilkinson Microwave Anisotropy Probe* and *Planck*, have opened a new window into the analysis of continuum emission from supernova remnants (SNRs). In this paper, different emission models that can explain the characteristic shape of currently known integrated radio/microwave continuum spectrum of the Galactic SNR IC 443 are tested and discussed. In particular, the possibility is emphasized that the slight bump in the integrated continuum of this remnant around 20–70 GHz is genuine and that it can be explained by the contribution of an additional emission mechanism such as spinning dust. We find that adding a spinning dust component to the emission model improves the fit of the integrated spectrum of this SNR while at the same time preserving the physically probable parameter values. Finally, models that include the high-frequency synchrotron bending of the IC 443 radio to microwave continuum are favored.

Key words: ISM: individual objects (IC 443) – ISM: supernova remnants – radiation mechanisms: general – radio continuum: ISM

1. INTRODUCTION

The radio-continuum spectra of supernova remnants (SNRs) are generally shaped by the (non-thermal) synchrotron radiation. In an external magnetic field B [μG], an electron of energy E [GeV] radiates its peak power at a frequency ν [GHz], according to the particular relation $E = 14.7\sqrt{\nu/B}$ (Reynolds 2008). That leads to the conclusion that, for the standard value of the mean Galactic magnetic field (of the order of 1 μG), GeV electrons are responsible for the observed synchrotron emission in the gigahertz range. The most probable and efficient mechanism for production of a high-energy particle ensemble in SNRs is diffusive shock acceleration (Bell 1978; Blandford & Ostriker 1978). It produces the non-thermal ensemble that in the simplest, test-particle case has a power-law energy distribution (see Urošević 2014 and references therein for a review). The analysis of the integrated radio to microwave continuum of SNRs (over a broad range of frequencies) is important because possible deviations from the theoretical predictions can give us new insights into the physics behind the observed radiation.

Generally, the verification of several theoretical models (e.g., nonlinear particle acceleration in young SNRs, significant thermal bremsstrahlung emission from SNRs expanding in a dense environment, models of dust emission linked to the SNRs, etc.) relies particularly on a good knowledge of the high-frequency part of the radio as well as the microwave continuum of SNRs (Reynolds & Ellison 1992; Scaife et al. 2007; Onić et al. 2012; Onić 2015; Onić & Urošević 2015; Génova-Santos et al. 2017). Ground-based radio observations of SNRs at frequencies higher than around 10 GHz generally suffer from transparency issues due to the existence of Earth's atmosphere. In that sense, high-altitude and/or space observatories are needed for the analysis of the high-frequency radio to microwave spectral range.

Recently, observations from the microwave survey of Galactic SNRs made by *Planck*[4] have become available (Planck Collaboration Int. XXXI 2016). *Planck* has made all-sky observations in nine frequency bands between 30 and 857 GHz. The Low Frequency Instrument on board *Planck* covered the 30, 44, and 70 GHz bands with angular resolutions of around 33′, 24′, and 14′, respectively (Mandolesi et al. 2010; Planck Collaboration VI 2016). The High Frequency Instrument, however, covered the 100, 143, 217, 353, 545, and 857 GHz bands with an angular resolution ranging from around 9.′9 to 4.′4 (Planck HFI Core Team VI 2011; Planck Collaboration VIII 2016). For a comparison, the angular resolution of the *Wilkinson Microwave Anisotropy Probe* (*WMAP*) at 23, 33, 41, 61, and 94 GHz is around 53′, 40′, 31′, 21′, and 13′, respectively (Bennett et al. 2003). That makes *WMAP* unsuitable for the analysis of most Galactic SNRs (see Green 2014). Only a few Galactic SNRs with large enough angular dimensions were detected with *WMAP* (Cas A, Puppis A, HB 21, W44 region; Weiland et al. 2011; Hewitt et al. 2012; Pivato et al. 2013; Irfan et al. 2015; Génova-Santos et al. 2017).

In this paper, the integrated continuum radio to infrared spectrum of SNR IC 443 is analyzed and the different emission models that can be responsible for its particular shape are tested. Section 2 is dedicated to the main characteristics of the remnant while Section 3 focuses on the properties of its radio/microwave continuum. Section 4 discusses different theoretical emission models that are appropriate in the analysis of this SNR. In particular, the hypothesis that the bump in the integrated continuum of SNR IC 443 around 20–70 GHz is genuine and that it can be explained by the contribution of additional emission such as from spinning dust is analyzed in

[4] *Planck* (http://www.esa.int/Planck) is a project of the European Space Agency (ESA) with instruments provided by two scientific consortia funded by ESA member states, with contributions from NASA (USA) and telescope reflectors provided by a collaboration between ESA and a scientific consortium led and funded by Denmark.

Section 5 and further discussed in Section 6. The final section summarizes the main results of the analysis.

2. SNR IC 443

The SNR IC 443 (G189.1+3.0, 3C 157), also known as the Jellyfish Nebula in the visible sky, has a rather large angular size in comparison with the majority of Galactic SNRs detected in the radio domain (45′; Green 2014). In addition to its apparent dimensions, its rough proximity to the location of the Galactic anti-center leaves this remnant relatively well isolated from the confusing effects that normally complicate studies of the inner Galactic SNRs (Castelletti et al. 2011; Ohnishi et al. 2014). A distance of 1.5 kpc (corresponding a diameter of 20 pc) is adopted in most papers related to IC 443, although this is still debated (Fesen 1984; Welsh & Sallmen 2003). In fact, this SNR also probably has a physical connection with the H II region SH 2-249 located north of IC 443, which leads to a slightly greater distance of 1.5–2 kpc (Reich et al. 2003; Gao et al. 2011). The age of this SNR is roughly estimated as 3000 to 30,000 years (Petre et al. 1988; Olbert et al. 2001; Leahy 2004), or a more precise age of 20,000 years was suggested in Lee et al. (2008).

This SNR has been extensively observed and analyzed throughout the whole electromagnetic spectrum from radio frequencies to γ-rays. IC 443 shows a limb-brightened morphology at optical, infrared, and radio wavelengths, while it manifests a centrally peaked morphology of thermal bremsstrahlung origin in X-rays (Kokusho et al. 2013a, and references therein). As a consequence, it has been classified as a mixed-morphology or thermal-composite SNR (Rho & Petre 1998). Robust evidence for the presence of recombining plasma is based on analysis of the X-ray emission of this remnant (Kawasaki et al. 2002; Yamaguchi et al. 2009; Ohnishi et al. 2014).

On the basis of the radio and X-ray morphology and spectral analysis, as well as the radio polarization properties, Olbert et al. (2001) found that the non-thermal X-ray source, located in the southern portion of IC 443, is a synchrotron nebula powered by a central compact point source (with a soft X-ray thermal spectrum that is consistent with emission from the surface of a neutron star; Bocchino & Bykov 2001). They also suggested that it is physically associated with IC 443. The existence of a pulsar wind nebula (Swartz et al. 2015) and a metal-rich X-ray plasma (Troja et al. 2008) would indicate that IC 443 originates from the core collapse of a massive progenitor star (Kokusho et al. 2013a), probably a 15–19 $\mathcal{M}_{\odot}$ B0 star (Su et al. 2014). Still, there remains some doubt as to the physical association of the pulsar wind nebula and the SNR IC 443 (Leahy 2004; Gaensler et al. 2006). So far, no pulsations have been detected from the neutron star.

SNR IC 443 is evolving in a rich and complex interstellar region. It interacts with both low- and high-density material, which strongly affects its evolution. It is a prototypical case of an SNR impacting dense interstellar molecular gas. In fact, it is associated with a dense giant molecular cloud (MC) near the Gem OB1 association (Cornett et al. 1977; Humphreys 1978; Heiles 1984). The SNR/MC interaction in IC 443 is very well studied (Hoffman et al. 2003; Shinn et al. 2011; Su et al. 2014; Kilpatrick et al. 2016, and references therein). Actually, the physical conditions toward this SNR are very well suited for all known shock interaction tracers that are traditionally used to identify SNR/MC interactions (broadened CO emission, OH 1720 MHz maser, HCO^+, HCN, H_2 emission, etc.). Furthermore, detection of the characteristic pion-decay feature in the γ-ray spectrum provides direct evidence that cosmic-ray protons (which penetrate high-density MCs) are indeed accelerated in SNRs (Abdo et al. 2010; Tavani et al. 2010; Ackermann et al. 2013; Tang & Chevalier 2014, 2015).

Oliva et al. (1999) found that IC 443 is characterized by prominent line-emitting filaments and relatively strong *IRAS* (*Infrared Astronomical Satellite*) 12 and 25 μm emission, with most of the flux accounted for by ionized line emission (mainly of [Ne II] and [Fe II]). They also noted the possible contribution of H_2 lines to the *IRAS* 12 μm flux from the southern rim of IC 443. In other words, Oliva et al. (1999) suggested that lines account for most of the *IRAS* 12 and 25 μm emission from the line-emitting filaments of IC 443. That is in contrast with the common interpretation involving thermal radiation from very small grains stochastically heated by collisions with the hot plasma behind the shock front. In addition, Kokusho et al. (2013a) have found that the [Fe II] line emission is enhanced relative to the thermal emission from the warm dust in the central region of IC 443. They concluded that ionized Fe, in that region, is probably mostly of interstellar rather than ejecta origin. Kokusho et al. (2013b) emphasized the possibility that the majority of Fe atoms are in fact contained in the deepest cores of dust grains, or that there is a population of Fe-rich dust that is relatively resistant to sputtering.

It is worth mentioning that Hezareh et al. (2013) reported the detection of levels of non-Zeeman circular polarization and linear polarization of up to 1% in the CO rotational spectral line emission in a shocked molecular clump around the SNR IC 443. They concluded that the non-Zeeman CO circular polarization is most probably due to a conversion from linear to circular polarization, consistent with a physical model based on anisotropic resonant scattering of Houde et al. (2013). In fact, it is proposed that background, linearly polarized CO emission interacts with similar foreground molecules aligned with the ambient magnetic field and scatters at a transition frequency. Actually, the difference in phase shift between the orthogonally polarized components of this scattered emission can cause a transformation from linear to circular polarization. Furthermore, Koo et al. (2010) measured the Zeeman splitting of the H I 21 cm emission line from shocked atomic gas in IC 443 and derived an upper limit of $B_{\|} = 100$–150 μG on the strength of the line-of-sight magnetic field component. They proposed that either the magnetic field is roughly random within the telescope beam due to inhomogeneities in preshock gas and/or various hydrodynamic instabilities—or alternatively the preshock density may be low, much lower than the mean density of molecular clouds. Koo et al. (2010) emphasized that the latter is possible if the molecular cloud with which the SNR is interacting is clumpy and the high-velocity H I emission is from the shocked diffuse interclump medium. Finally, as the radio spectral index of this remnant (see Equation (1) and Section 3) is less than the characteristic value of 0.5, we cannot use the standard method, i.e., the equipartition calculation (see Arbutina et al. 2012, 2013 for more details), to estimate the magnetic field strength.

3. THE RADIO/MICROWAVE CONTINUUM OF SNR IC 443

Two main subshells (shells A and B), with markedly different radial intensity distributions, make up the majority of

the SNR IC 443 in radio-continuum emission (Braun & Strom 1986; Reich et al. 2003; Leahy 2004). They appear to be connected, roughly spherical, half-shells of radio synchrotron emission, which are centered at different spatial positions. Together, they define the usually assumed boundaries of the SNR. Shell A appears brighter, limb-brightened, and is coincident with the molecular shock tracers along its southern boundary and across the center of the SNR as a whole (Kilpatrick et al. 2016). Shell B, however, is dimmer and has predominantly uniform surface brightness with some enhancement, the position of which coincides with the optical filaments (Lee et al. 2008). The radius of shell A is around 19′ or 8.3 pc and that of shell B is around 29′ or 12.7 pc, for the assumed SNR distance of 1.5 kpc (Leahy 2004). The nature of a third, larger, incomplete, and faint shell extending beyond the northeast periphery of the remnant is still not clear enough although. It was proposed to be a different SNR (G189.6+3.3) that overlaps with IC 443 (Asaoka & Aschenbach 1994; Leahy 2004; Castelletti et al. 2011).

The radio morphology of IC 443 described above is consistent with the scenario whereby the western part of the remnant has actually broken out into a rarefied medium (Lee et al. 2008). In fact, it is proposed that the SNR has probably been formed inside a dense medium (possibly evolved inside the pre-existing wind-blown bubble) and then broken out into the adjacent rarefied medium. In addition, Su et al. (2014) reported infrared detection of 62 young stellar object (YSO) candidates (disk-bearing young stars: 24 of Class I and 38 of Class II), mainly concentrated along the boundary of the remnant's bright radio shell (but absent from the southwestern breakout portion of the SNR), and suggested that they are likely to be triggered by the stellar wind from the massive progenitor of SNR IC 443.

The integrated radio-continuum spectrum of SNRs (integrated flux density versus frequency) is generally represented by a simple power law that arises from the synchrotron emission of electrons accelerated by a diffusive shock acceleration mechanism:

$$S_\nu^{\rm syn} \propto \nu^{-\alpha}, \quad (1)$$

where α is the radio spectral index.

The intensity of radio synchrotron emission depends mainly on the energy of non-thermal electrons and the magnetic field strength. Generally, for radiative shocks (usually present in mixed-morphology SNRs), the compression factors are large, giving rise to strongly compressed magnetic fields and increased cosmic-ray electron densities. For steady radiative shocks propagating through a uniform medium with a certain number density of hydrogen nuclei of preshock gas n_0 [10 cm^{-3}], the strength of the magnetic field $B_{\rm max}$ [μG] normal to the shock velocity $v_{\rm s}$ [100 km s^{-1}] reaches $B_{\rm max} \approx 240\ v_{\rm s}\ \sqrt{n_0}$ (Chevalier 1974). As a result, the radio synchrotron emission from dense SNR shells is enhanced (van der Laan mechanism; van der Laan 1962). In fact, the emitting electrons may be either those accelerated by the SNR or simply ambient relativistic electrons swept up by the radiative shocks (Vink 2012). Of course, the radio emission may be additionally enhanced by the presence of secondary electrons/positrons, i.e., the products left over from the decay of charged pions, created by cosmic-ray nuclei colliding with the background plasma (Uchiyama et al. 2010). Finally, models that assume that the energy spectrum of the non-thermal electrons is shaped by the joint action of first- and second-order Fermi acceleration (Ostrowski 1999) in a turbulent plasma with substantial Coulomb losses were also proposed and tested for the case of SNR IC 443 (see Bykov et al. 2000 for more details).

This remnant also exhibits a turnover in its integrated radio-continuum spectrum at the lowest frequencies (below around 30 MHz). Contrary to the expectation that such absorption arises from unrelated low-density H II regions (or their envelopes) along the line of sight, Castelletti et al. (2011) proposed that in this case the absorbing medium is directly linked to the SNR itself. Evidence for a similar situation has also been observed in the case of 3C 391 (Brogan et al. 2005). Castelletti et al. (2011) reported the excellent correspondence between the observed eastern radio region that had the flattest spectrum (the spectral index actually varies across the SNR) and near-infrared ionic lines, which strongly suggests that the passage of a fast, dissociating J-type shock across the interacting molecular cloud actually dissociated the molecules and ionized the gas. They therefore concluded that such a collisional ionization is responsible for the thermal absorbing electrons that produce the peculiar areas with a very flat spectrum that are observed all along the eastern border of IC 443. This is in agreement with the model proposed by Rho et al. (2001) in which the infrared emission from the ionized species in the eastern bright radio limb of IC 443 comes from shattered dust produced by a fast dissociating J-type shock. Assuming an electron temperature in the range between 8000 and 12,000 K (consistent with infrared analysis), Castelletti et al. (2011) estimated an emission measure of (2.8–5.0) $\times$ 10^3 cm^{-6} pc for the region with the strongest thermal absorption (eastern rim).

The flux density of the already mentioned pulsar wind nebula in IC 443 at 1.42 GHz is 0.20 $\pm$ 0.04 Jy, while the integrated flux density of the SNR is around 140 Jy at the same continuum frequency (Castelletti et al. 2011).

Finally, Planck Collaboration Int. XXXI (2016) reported detection of the SNR IC 443 at all nine *Planck* frequencies and suggested that the spectral energy distribution across radio and microwave frequencies can be reasonably approximated by a combination of synchrotron and dust emission. They noted that the synchrotron emission roughly follows a power law with a radio spectral index of 0.36 from radio frequencies above 30 MHz up to 40 GHz, after which the spectral index steepens to 1.56. It is proposed that the decrease in flux density could be due to a break in the synchrotron power law from the injection mechanism of the energetic particles, or due to losses from cooling of the energetic particles. The higher-frequency emission was found to be most likely due to dust grains that survive the shock. No indications of significant thermal bremsstrahlung emission from the SNR have been found by Planck Collaboration Int. XXXI (2016), in contrast to the results of Onić et al. (2012).

However, there is a slight bump seen in the radio to microwave integrated continuum spectrum of this SNR, as known at present, around 20–70 GHz (see Figures 2 and 3). That can be an indication of the significant presence of some other emission mechanism (such as of spinning dust emission), which is discussed bellow.

4. THE EMISSION MODELS

To account for the low-frequency spectral turnover, due to the thermal (free–free) absorption, and possible thermal bremsstrahlung emission, one can, generally, assume several

models. One such model assumes that thermal absorption and emission actually originate from the same volume of space, just ahead of the region that emits synchrotron radiation. If the frequencies are given in gigahertz, we can write

$$S_\nu^{\rm M1} = S_\nu^{\rm syn}\exp[-\tau_\nu] + S^{\rm ff}\nu^2(1-\exp[-\tau_\nu]), \quad (2)$$

where $\tau_\nu \propto \nu^{-2.1}$ is an optical depth, $S_\nu^{\rm syn}$ is given by Equation (1), and $S^{\rm ff}$ corresponds to the thermal (free–free) flux density at 1 GHz. On the other hand, if we assume that both thermal absorption and emission, as well as the synchrotron radiation, are coming from the same region, we have

$$S_\nu^{\rm M2} = (S_\nu^{\rm syn}/\tau_\nu + S^{\rm ff}\nu^2)(1-\exp[-\tau_\nu]). \quad (3)$$

In order to estimate the initial value of the parameter $S^{\rm ff}$ for the least-squares fits (see Section 5) in the case of SNR IC 443, one can use the electron temperatures derived in Castelletti et al. (2011) and the value of 10^{-4} sr for the source solid angle $\Omega_{\rm S}$ (Green 2014) in the formula $S^{\rm ff} = 2k_{\rm b}T_{\rm e}\Omega_{\rm S}/c^2$, where $k_{\rm b}$ and c are the Boltzmann constant and the speed of light, respectively.

Of course, one should bear in mind that SNRs are in essence 3D structures, which is the main drawback of these models. Also, the possibility of synchrotron self-absorption is not discussed here. It is generally very hard to discriminate between thermal absorption effects (in an optically thick region, the spectral index is $\alpha = 2$) and synchrotron self-absorption ($\alpha = 2.5$). However, Castelletti et al. (2011) showed that the main effect responsible for the low-frequency spectral turnover, in the case of SNR IC 443, comes from the thermal absorption that is associated with this SNR.

Thermal dust emission, which dominates the continuum spectrum of IC 443 above 140 GHz, is usually very well described by the simple model represented by a modified blackbody relation:

$$S_\nu^{\rm Td} \propto \nu^{\beta_{\rm d}} B_\nu(T_{\rm d}), \quad (4)$$

where $B_\nu(T_{\rm d})$ is the standard Planck blackbody function for dust at temperature $T_{\rm d}$ and $\beta_{\rm d}$ is the (dust) emissivity index, with a value usually between 0 and 2 (Blain et al. 2002; Planck Collaboration XI 2014). Planck Collaboration Int. XXXI (2016) used *Planck*'s data and fitted thermal dust emission with a one-temperature model. They estimated a dust temperature of 16 K with emissivity index of 1.5, but as they noted, the precise values are not unique and require combination with infrared data and multiple-temperature components given the complex mixture of dust in molecular, atomic, and shocked gas. On the other hand, Saken et al. (1992) fitted only *IRAS* infrared data with a two-temperature model with (both) emissivity indices of 1.5, and estimated temperatures of the cold and hot dust components of 34.3 and 185 K, respectively. They used only the observed fluxes in the fitting procedure and not the color-corrected fluxes, since the color-correction factors are themselves model-dependent. It should be noted that there is a large disagreement regarding the true infrared flux densities in the literature, especially at 12 and 25 μm (see Table 6 in Saken et al. 1992).

In addition, spinning dust emission can shape the continuum spectra in the form of a characteristic bump between 10 and 100 GHz (Erickson 1957; Draine & Lazarian 1998a, 1998b). This is electric dipole emission from very small grains that spin rapidly due to the action of systematic torques in the interstellar medium (ISM). This emission mechanism is currently one of the most probable proposed mechanisms to explain the so-called anomalous microwave emission (AME), i.e., dust-correlated emission from the Milky Way, observed around 10–100 GHz, that cannot be accounted for by extrapolating the thermal dust emission to low frequencies (Planck Collaboration Int. XV 2014, and references therein). The analysis of AME is of great importance because studies of the cosmic microwave background consider AME as an additional source of foreground contamination. Scaife et al. (2007) asserted for the first time the possibility of significant spinning dust emission from the vicinity of the SNR 3C 396. In contrast, using new Parkes 64 m telescope observations, Cruciani et al. (2016) found that currently known integrated continuum data do not favor the presence of either this emission component or thermal bremsstrahlung radiation. Finally, based on the new *Planck* data, Onić (2015) proposed that the spinning dust mechanism can account for a significant excess emission at 30 GHz from the vicinity of SNR W44. Furthermore, Génova-Santos et al. (2017) found very compelling evidence for spinning dust emission associated with W44.

Spinning dust emission is a very complex process. It actually depends on the size, shape, and charge of the emitting dust grains. This emission mechanism also depends on the environmental conditions such as gas temperature, molecular fraction, ionization state, and the intensity of the radiation field (Ali-Haïmoud et al. 2009; Hoang et al. 2010, 2011; Ysard & Verstraete 2010; Ysard et al. 2010, 2011; Silsbee et al. 2011; Ali-Haïmoud 2013; Hoang & Lazarian 2016). A simple expression (that much simplifies the underlying physics) can be written as

$$S_\nu^{\rm Spd} \propto (\nu/\nu_0)^2\exp[1-(\nu/\nu_0)^2], \quad (5)$$

where ν_0 is the peak frequency, usually between 10 and 70 GHz (Draine & Hensley 2012; Hensley et al. 2015). More robust analysis can be performed using more advanced numerical schemes, e.g., `SpDust` code, ver. 2.01 (Ali-Haïmoud et al. 2009; Silsbee et al. 2011) or more realistic approximations such as that of Stevenson (2014):

$$\begin{aligned} S_\nu^{\rm Spd} \propto\ & (\nu/\nu_0)^{c_1}\exp[-0.5\,c_2\ln^2(\nu/\nu_0)] \\ & \times \mathrm{erfc}[c_3\ln(\nu/\nu_0)+c_4], \end{aligned} \quad (6)$$

where c_i are particular model parameters (see Stevenson 2014 for details).

Hensley et al. (2016) emphasized that the emission from spinning ultrasmall grains might be enhanced in SNRs if shattering in grain–grain collisions increases the population of ultrasmall grains, or suppressed if ultrasmall grains are destroyed by sputtering. In fact, several processes can excite or dampen a grain's rotation: gas/grain interactions, photon emission (infrared and radio), formation of H_2 molecules on the grain surface, or photoelectric emission (Planck Collaboration XXI 2011). Moreover, the interstellar radiation field strongly affects the composition of the ISM, since it can not only charge but also destroy dust grains when the intensity is high enough (Planck Collaboration Int. XV 2014).

Finally, it is known that the integrated radio-continuum spectra of some dynamically evolved Galactic as well as several extragalactic SNRs could appear in a (high-frequency) concave-down form (see Urošević 2014 for a review). A few examples of Galactic SNRs with such radio spectra can be found in the recent

literature, e.g., the cases of SNRs S147, HB 21, W44, IC 443, Puppis A, etc. (Xiao et al. 2008; Hewitt et al. 2012; Pivato et al. 2013, Planck Collaboration Int. XXXI 2016). Within the sample of SNRs whose spectra show such spectral breaks there are examples that range from bright to faint and from young to mature objects. The sample also includes SNRs with and without compact stellar remnants. Such spectral shapes may be caused by a combination of cosmic-ray acceleration by the shocks and pulsars, deceleration in denser environments, as well as aging (Leahy & Roger 1998; Reynolds 2009, Planck Collaboration Int. XXXI 2016, and references therein). In the case of some Large Magellanic Cloud SNRs, observed spectral breaks are explained by the effect of coupling between synchrotron losses and observational constraints (resolution) when the distant (extragalactic) emission region remained unresolved (Bozzetto et al. 2010, 2012, 2013; de Horta et al. 2012).

Although they are just rough mathematical approximations, several simple expressions have been used to fit those continuum spectra that manifest such spectral breaks. One such an expression is the simple smooth broken power law:

$$S_\nu^{\rm syn} \propto (\nu/\nu_{\rm b})^{-\alpha_1}(1 + (\nu/\nu_{\rm b})^{\Delta\alpha})^{-1}, \quad \Delta\alpha = \alpha_2 - \alpha_1 > 0, \tag{7}$$

where α_1 and α_2 are particular spectral indices (for lower and higher frequency regimes) and $\nu_{\rm b}$ is the frequency at the spectral break. The simple exponential cut-off is another (see, e.g., Pivato et al. 2013):

$$S_\nu^{\rm syn} \propto \nu^{-\alpha} \exp[-\nu/\nu_{\rm c}], \tag{8}$$

where $\nu_{\rm c}$ is the characteristic cut-off frequency.

It should be emphasized, at this point, that the observed synchrotron X-ray emission from the rims of several young supernova remnants allows us to study the high-energy tail of the energy distribution of electrons accelerated at the shock front. Although synchrotron emission from the shock has not been detected in the X-ray observations of the SNR IC 443, it should be noted that, in general, the analysis of such non-thermal X-ray emission of mixed-morphology SNRs can provide information on the physical mechanisms that limit the energy achieved by the electrons in the acceleration process. Different physical mechanisms can be invoked to limit that maximum energy achieved by the electrons in the acceleration process, such as radiative losses, limited acceleration time available, and a change in the availability of magnetohydrodynamic waves above some wavelength (i.e., loss-limited, time-limited, and escape-limited scenarios; Reynolds 1998, 2008; Zirakashvili & Aharonian 2007; Vink 2012; Miceli et al. 2013, 2014; Pohl et al. 2015). If synchrotron losses of electrons occur uniformly over the whole lifetime of the SNR, t [10^4 yr], for magnetic field intensity B [10 μG], the high-frequency turnover would happen at the cut-off frequency $\nu_{\rm c}$ [MHz] $= 3.4 \times 10^9\ B^{-3}\ t^{-2}$ (Xiao et al. 2008). Finally, most recently, Auchettl et al. (2016) reported the detection of a non-thermal X-ray emission component from the mixed-morphology SNR G346.6-0.2 that is interacting with a molecular cloud. They concluded, surprisingly, that this is most likely synchrotron emission produced by the particles accelerated at the shock.

5. ANALYSIS AND RESULTS

The radio/microwave continuum data (the flux densities at different frequencies) for SNR IC 443 were taken from Table 2 of Castelletti et al. (2011), Table 1 of Gao et al. (2011), Table 3 of Reich et al. (2003), and Table 3 of Planck Collaboration Int. XXXI (2016). The flux densities at frequencies higher than 408 MHz that could not be corrected to the scale of Baars et al. (1977), i.e., where the correction factor was not available, were excluded from the analysis (see Table 2 in Castelletti et al. 2011). In addition, the *IRAS* infrared data point at 100 μm, taken from Table 3 of Saken et al. (1992), was included in the analysis because it gives us information on the "Wien side" of the thermal dust emission spectrum (although its associated relative error is around 14% and there is a modest disagreement between the flux density values stated in the various literature—see Table 6 from Saken et al. 1992).

The large scatter, even for data points at the same continuum frequencies, is apparent (see Figure 2 of this paper or Figure 7 from Castelletti et al. 2011). Generally, one should be very cautious in comparing data from different types of radio observations, e.g., single-dish versus interferometer. One should ensure that the measured flux densities can be reliably compared. In fact, to draw firm quantitative conclusions from such a combination of data (combined data sample) is very hard and can be rather biased. Another related drawback is that the flux densities at different frequencies were obtained from observations at different angular resolutions and using different techniques. In general, there could be completely different background contributions at different frequencies. One proposed strategy is to degrade all the maps to the same angular resolution, and use the same aperture size for all the frequencies as in Génova-Santos et al. (2017) for the case of SNR W44. Nevertheless, we stay in a framework of qualitative interpretation and stress the fact that the integrated radio/microwave emission from SNR IC 443, as presented in the known literature, cannot be explained solely by a combination of synchrotron and thermal dust emission.

To show that the observed high-frequency radio and microwave continuum of SNR IC 443 manifests a genuine bump around 30 GHz, one can apply principal component analysis (PCA; Babu & Feigelson 1996). The principal components are actually the eigenvectors of the covariance matrix. The original data can be represented in the (new) basis formed by these vectors. The role of the first principal component is that it accounts for as much of the variability in the data as possible. In fact, it has the largest possible variance. In other words, the eigenvector with the largest eigenvalue is the direction along which the data set has the maximum variance. The second principal component has the highest variance possible under the particular constraint of orthogonality to the first one. Moreover, the PCA allows calculation of the direction of highest data variability. That fact can be used to detect slight departures from the pure power-law spectra, i.e., a linear function on a log–log scale

Figure 1 shows the results of PCA applied to logarithmically transformed original data ($\log\nu$, $\log S_\nu$) at frequencies between 400 MHz and 143 GHz. These are high enough continuum frequencies such that the effects of low-frequency spectral bending can be neglected. The abscissa (PC1) and ordinate (PC2) correspond to the first and second principal component directions, respectively. Plotted values are the (original) data represented in the (new) basis of principal components (zero-

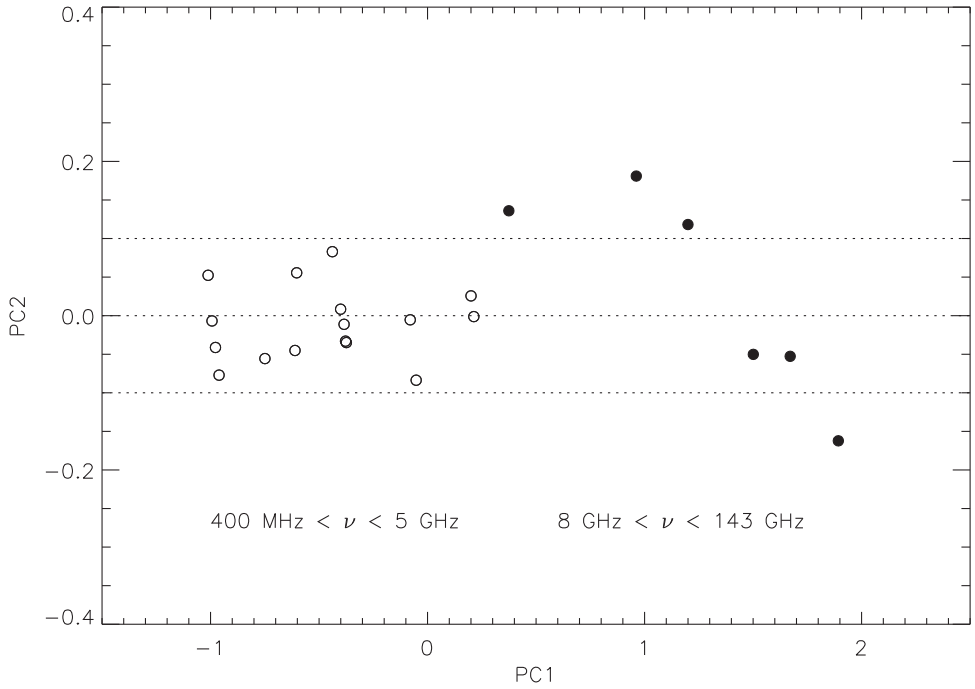

Figure 1. Results of PCA on logarithmically transformed data ($\log \nu$, $\log S_\nu$) for SNR IC 443. The abscissa (PC1) and ordinate (PC2) correspond to the first and second principal component directions, respectively. Plotted values represent the (original) data in the basis of principal components (zero-centered data multiplied by the rotation matrix whose columns contain the eigenvectors). The results of PCA on the data between 400 MHz and 5 GHz are marked with open circles. A slight departure from a linear relationship is obvious only when the data points between 8 and 143 GHz are included (filled circles).

centered data multiplied by the rotation matrix whose columns contain the eigenvectors). The covariance of these values represents a diagonal matrix with squares of standard deviations of the eigenvalues of the principal components as its elements. It is clear that the radio spectrum follows a pure power-law relation (a linear relation on a log–log scale) in the range between around 400 MHz and 5 GHz, although with undoubted scatter (open circles). Such a scatter is, in fact, expected due to the nature of the combined data sample as previously discussed. On the other hand, addition of the data points between 8 and 143 GHz (filled circles in Figure 1) shows that the continuum spectrum of IC 443 deviates slightly from the simple power law in that frequency range. In particular, the data point at 8 GHz, listed in Table 2 of Castelletti et al. (2011) and derived in the paper of Howard & Dickel (1963), has a large relative error of 20% (the first filled circle on the left). In fact, that does not favor the hypothesis of a genuine bump (with a physical origin). However, five *Planck* data points, between 30 and 143 GHz, have much smaller uncertainties (relative errors roughly between 5% and 8%). Not only is the slight positive curvature (excess emission) around 30 GHz apparent but also the slight concave-down feature (a dip in emissivity) at around 143 GHz is also clearly visible (filled circles in Figure 1). The latter can be easily explained by the change in shape of the synchrotron spectrum as discussed at the end of Section 4. As the continuum spectrum above 143 GHz is influenced by the thermal dust emission (deviation from the synchrotron power-law spectrum is a priori excepted), it was not of interest for the presented PCA analysis.

The surroundings of SNR IC 443 are composed of a very large number of interacting environments, such as molecular clouds, warm ionized medium, warm neutral medium, etc. Due to the low quality of the overall radio/microwave spectrum of this remnant (large scatter in the combined data sample used in the analysis; significant number of data points with relative errors as high as 20%) we confine ourselves to a qualitative analysis. In fact, distinguishing between different models is not at all trivial from currently available data. In that sense, the following, simplified models were used to describe the radio to microwave spectral energy distribution of the SNR IC 443:

$$S_\nu^i = S_\nu^{\mathrm{M}i} + S_\nu^{\mathrm{Spd}} + S_\nu^{\mathrm{Td}}(\beta_\mathrm{d}, T_\mathrm{d}), \tag{9}$$

where i (= 1 or 2) is used to represent Model 1 or Model 2, defined by Equations (2) and (3), respectively. We used Equation (8) to describe the high-frequency spectral bending. The thermal dust is fitted by the oversimplified model that assumes one modified blackbody (Planck-like) function (Equation (4)) in accordance with Planck Collaboration Int. XXXI (2016). We also use a simple representation for the spinning dust emission, given by Equation (5), due to the impossibility of a clear breaking of the degeneracies between slightly different models.

The procedure of a weighted least-squares fit is conducted by the `MPFIT`[5] (Markwardt 2009) package written in `IDL` throughout this paper, with starting values estimated from the data. We note that `MPFIT` provides estimates of the 1σ uncertainties for each parameter (the square root of the diagonal elements of the parameter covariance matrix).

Figures 2/3 show the weighted least-squares fit to the data when models M1/M2 are applied. Solid and dashed lines represent the fits with and without an additional component from spinning dust emission, respectively. Diamond symbols indicate *Planck* data, and the *IRAS* point at 100 μm is shown as a triangle. The data points with larger uncertainties have smaller weights, which is clearly seen in the results (see

[5] http://purl.com/net/mpfit

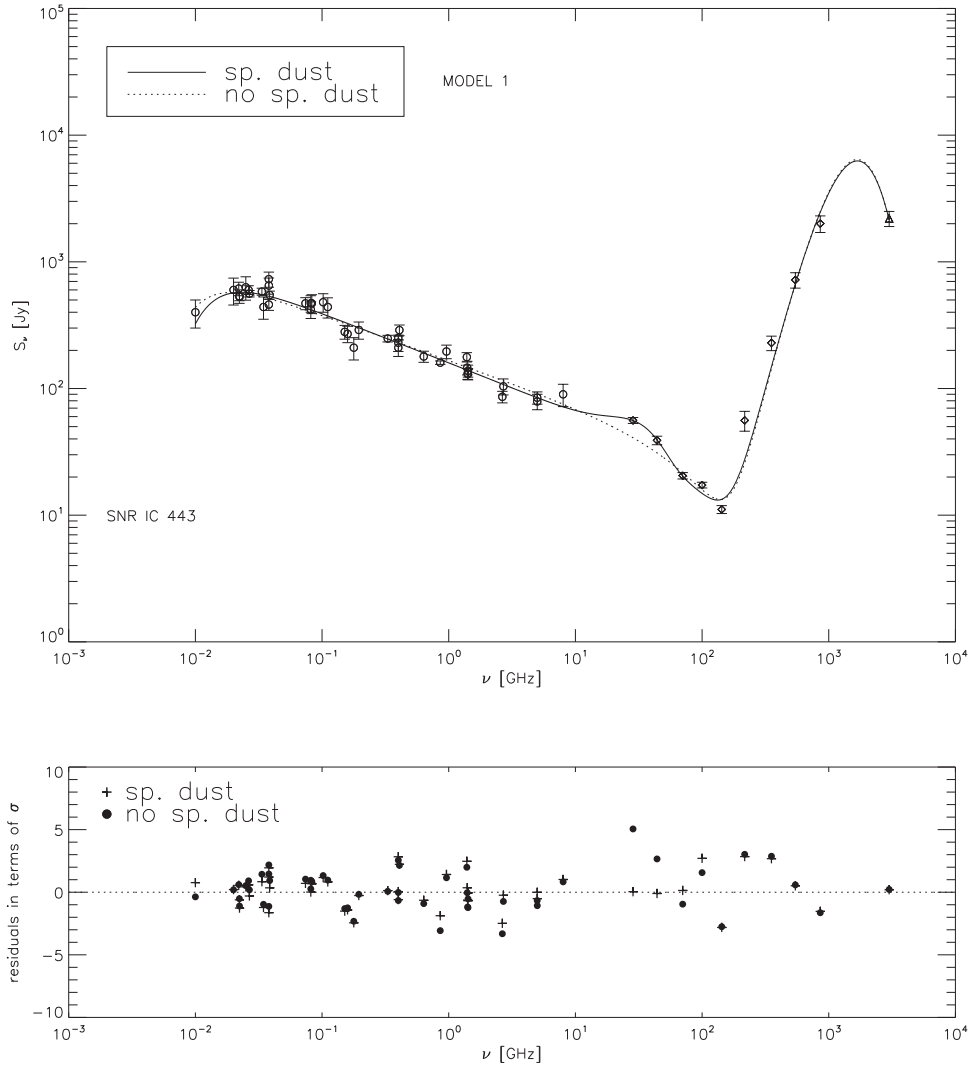

Figure 2. Weighted least-squares fit to the data for the model M1. The solid line represents the fit when spinning dust emission is included, while the dashed line corresponds to the fit without it, for comparison. Diamond symbols indicate *Planck* data and the *IRAS* point at 100 μm is shown as a triangle. In the lower graph, residuals in terms of the particular data uncertainties (σ) are presented: plus symbols and filled circles denote for the model with and without spinning dust emission, respectively.

Figures 2/3). Residuals (the difference between the observed value and the model prediction) in terms of the particular data uncertainties (σ) are presented In the lower graphs of Figures 2 and 3: plus symbols and filled circles are for the model with and without spinning dust emission mechanism, respectively. It is evident that the particular excess in flux density at around 30 GHz is very well explained by the addition of the component from spinning dust emission. In fact, when the spinning dust component is included, the data point at 28.5 GHz deviates by only around 0.04σ (model M1) and 0.7σ (model M2) from the predicted values, which is very well inside the general scatter that is present in the data (see Figures 2/3). On the other hand, in the case of a fit without any additional emission mechanism, the same data point deviates slightly more than 5σ from the predicted value (for both models M1 and M2). However, data points at 100 and 143 GHz still depart significantly from the predicted values even in the case of fits with spinning dust emission included (their residuals are beyond the uppermost ones, i.e., those at 178 MHz and 408 MHz, with associated relative errors of around 20% and 10%, respectively—Bennett 1962; Colla et al. 1971). The simple explanation can be found in the fact that both the synchrotron cut-off and the thermal dust emission model should, in fact, be represented by more realistic (complicated) functions as discussed earlier. In addition, the *Planck* data point at 217 GHz (with rather large relative uncertainty of around 18%; Planck Collaboration Int. XXXI 2016) also deviates slightly from the model predictions, which is yet another indication that this part of the continuum should be represented by more advanced models (two-temperature modified blackbody thermal dust emission, more physically justifiable functions representing the synchrotron high-frequency cut-off). As the uncertainty in the background subtraction generally makes it difficult to measure the flux density accurately, the lack of good quality data, especially in the infrared range, permits such an analysis. Nevertheless, whether it is just contamination from a complex nearby region or possibly genuine radiation from the SNR, spinning dust emission can very well account for the apparent excess emission in the currently presented integrated continuum of IC 443 at frequencies around 20–70 GHz.

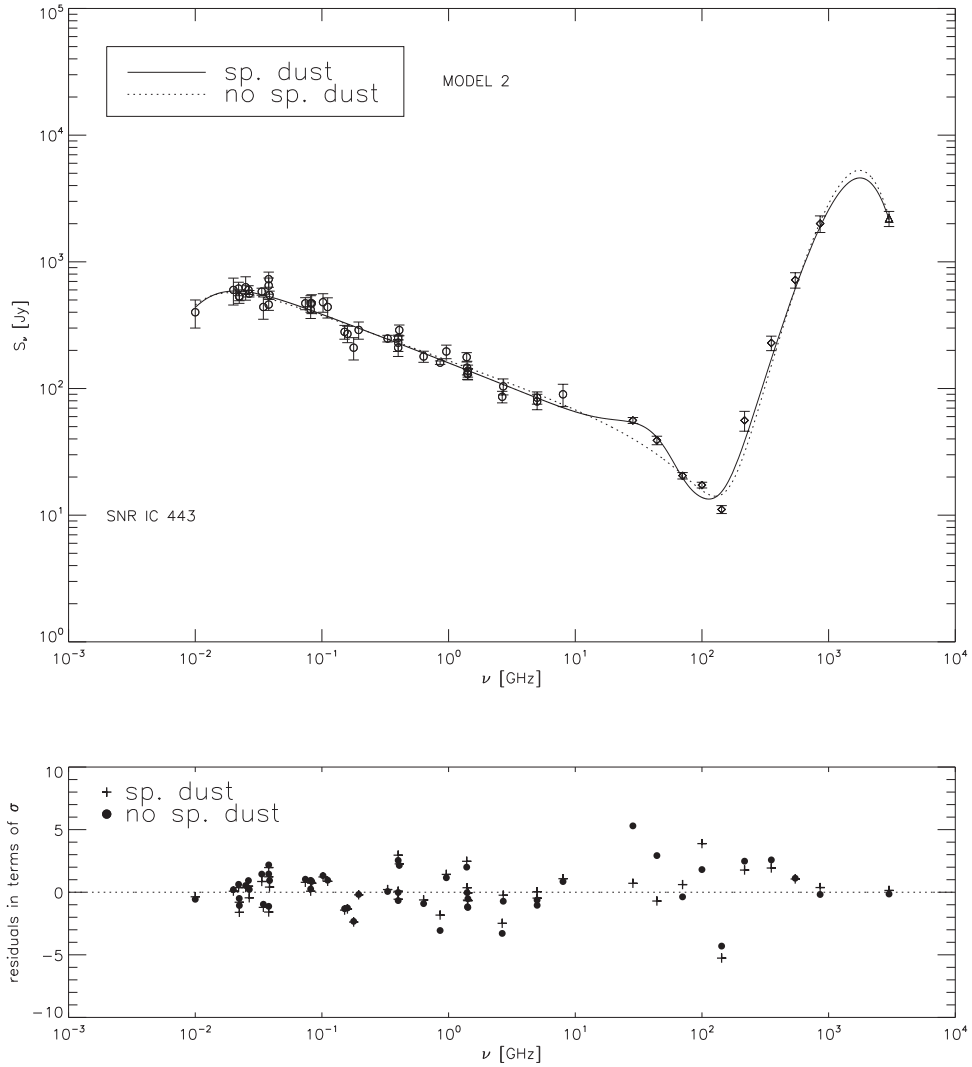

Figure 3. Weighted least-squares fit to the data for the model M2. The solid line represents the fit when spinning dust emission is included, while the dashed line corresponds to the fit without it, for comparison. Diamond symbols indicate *Planck* data and the *IRAS* point at 100 μm is shown as a triangle. In the lower graph, residuals in terms of the particular data uncertainties (σ) are presented: plus symbols and filled circles denote the model with and without spinning dust emission, respectively.

Table 1
The Best Fitting Parameters for Analyzed Models

Model	α	ν_c (GHz)	$f(30)$	ν_0 (GHz)	T_d (K)	β_d	χ^2 (k)
M1 with sp. dust	0.39 ± 0.01	152 ± 24	0.36	28 ± 3	15.2 ± 0.9	2.34 ± 0.23	95 (42)
M1 without sp. dust	0.35 ± 0.01	129 ± 15	…	…	14.9 ± 0.9	2.43 ± 0.23	138 (44)
M2 with sp. dust	0.38 ± 0.01	112 ± 16	0.37	32 ± 3	18.5 ± 1.4	1.64 ± 0.21	115 (42)
M2 without sp. dust	0.36 ± 0.01	120 ± 13	…	…	17.0 ± 1.4	1.97 ± 0.30	146 (44)

The best fitting parameters for the analyzed models are presented in Table 1, namely the radio synchrotron spectral index α, (synchrotron) cut-off frequency ν_c, spinning dust fraction $f(30)$ (ratio between the estimate of the spinning dust flux density at 30 GHz, $S^{Spd}(30)$, and the total flux density at the same frequency: $f(30) = S^{Spd}(30)/S(30)$), peak frequency ν_0, temperature of the thermal dust T_d, emissivity index β_d, and the values of χ^2. In Table 1, the parameter $k = N - p$ (where N is the number of data points and p is the number of model parameters) is given for convenience. One should also bear in mind that in nonlinear models k does not always represent the exact number of degrees of freedom, which is generally unknown, i.e., it is not possible to compute the exact value of reduced χ^2 (Andrae et al. 2010). Nevertheless, it is clear that the fits with model M1 have somewhat smaller χ^2 for the same k than those with model M2.

It is worth noting that our model predictions for thermal dust parameters (taking the error estimates into account) are in general accordance with those for Galactic clouds (see, e.g., Table 3 from Planck Collaboration Int. XV 2014). Still, model M1 predicts a rather unusually high emissivity index $\beta_d > 2$ for both cases, with and without spinning dust emission (but see the discussion on the radio continuum of YSOs driving known outflows; AMI Consortium et al. 2012), although other

parameters of model M1 do not deviate significantly from the results of model M2. Of course, it is highly probable that this discrepancy comes from the (already discussed) oversimplification of the continuum emission above about 70 GHz.

Our fits also do not favor a significant contribution from the thermal bremsstrahlung emission component. In addition, if we exclude the infrared data point at 100 μm, the fits degrade in quality although the results do not change significantly from those presented. Finally, the rather large values of χ^2 (see Table 1) are not at all surprising if we keep in mind (1) the large scatter in data points and (2) the simplified models used.

The radio synchrotron spectral index agrees well with the results of Planck Collaboration Int. XXXI (2016), although they did not assume the low-frequency bending (thoroughly discussed in Castelletti et al. 2011) because they did not fit the entire radio continuum (from the lowest frequency measurement at 10 MHz with a rather high relative uncertainty of 25%; Bridle & Purton 1968). Actually, they used the simple broken power law as a model of synchrotron radiation in addition to the component for one modified blackbody (MBB) to represent the thermal dust emission. For a comparison, we modeled our data sample with a smooth broken power law (Equation (7)) and one MBB component (Equation (4)). Although the fit is not of significantly lower quality ($\chi^2 = 132$, $k = 45$) than the results presented in Table 1, the high-frequency spectral index α_2 has a rather high value of around 3 ($\alpha_1 = 0.34 \pm 0.01$, $\Delta\alpha = 2.70 \pm 0.48$, $\nu_b = 84 \pm 4$). This is much higher than the values considered in the theory that supports the proposition that the breaks in spectral index are consistent with synchrotron losses of electrons injected by a central source (see, e.g., Reynolds 2009). This model also does not take into account the low-frequency thermal absorption effects.

We should also note that fits without high-frequency synchrotron spectral steepening are not favored. However, using our data sample we cannot thoroughly distinguish between synchrotron models that incorporate a smooth broken power law and those with an exponential cut-off.

Finally, we would also like to point out that there is a significant difference between the data sample used by Planck Collaboration Int. XXXI (2016) and the one presented in this paper. The former used only the data above 1 GHz (in fact, only six data points taken from Table 2 of Castelletti et al. (2011) in addition to the *Planck* measurements). They also used the data for which a correction factor to the scale of Baars et al. (1977) was unavailable, e.g., they included the 10.7 GHz point from Kundu & Velusamy (1972). These differences are important because they may change the conclusions significantly.

6. DISCUSSION

Additional support for the hypothesis of spinning dust emission can be found in certain correlations with thermal dust emission, especially at *IRAS* wavelengths. In particular, Planck Collaboration Int. XV (2014) found that the 12 μm/25 μm intensity ratio for spinning dust emission sources is usually about 0.6–1.0. For various observations of IC 443 at these wavelengths (see Table 6 from Saken et al. 1992), this leads to around 0.6–0.9 for the SNR IC 443, which is in agreement with above predictions. However, ionic line contamination of the particular *IRAS* bands, as emphasized in Oliva et al. (1999), makes this correlation uncertain. Another known indicator is the ratio between the estimate of spinning dust flux density at 30 GHz and the flux density at 100 μm (3000 GHz), which is usually around (1–15) $\times 10^{-4}$ (Planck Collaboration Int. XV 2014; Hensley et al. 2016). Bearing in mind the roughness of our analysis, we obtained larger values in the range (90–100) $\times 10^{-4}$, for both models used in this paper and various infrared observations from the literature. In addition, spinning dust fractions for both models are slightly less than $f(30) \approx 0.5$ (see Table 1), which was found in Planck Collaboration Int. XV (2014) for the known AME regions.

One should also consider the possible contribution of ultracompact H II regions (UCH II) to the detection of diffuse AME. At low frequencies, typically below 15 GHz, these objects may be optically thick, moving into the optically thin regime at frequencies higher than 15 GHz (Irfan et al. 2015). If a UCH II region, optically thick at 5 GHz, is positioned within the observed source region this would result in what would appear to be excess emission at higher frequencies where the UCH II region becomes optically thin. To ensure that the excess emission seen around 30 GHz is due to the spinning dust, the source region must be checked for nearby optically thick UCH II regions. We used the *IRAS* Point Source Catalog (Beichman et al. 1988) to identify such objects in a region of radius 1° around the established central coordinates of IC 443. In fact, UCH II regions generally possess *IRAS* color ratios of $\log(S_{60\mu m}/S_{12\mu m}) \geqslant 1.30$ and $\log(S_{25\mu m}/S_{12\mu m}) \geqslant 0.57$, which can be used as a way to identify these objects (Wood & Churchwell 1989; Dickinson 2013, Planck Collaboration Int. XV 2014). Extragalactic sources, as well as those with only upper limits for the *IRAS* fluxes listed, were excluded. No sources were found to match all the criteria.

We want to emphasize the importance of discrimination between the free–free emission from YSOs and spinning dust emission (Scaife 2012). YSOs can generate emission at centimeter wavelengths due to a variety of mechanisms such as stellar winds and/or shock-induced ionization, which can mimic the spectral signal of spinning dust emission (AMI Consortium et al. 2010; Tibbs et al. 2015). In fact, understanding whether the observed sources are both simultaneously forming stars and harboring spinning dust emission can help us to understand the potential role of spinning dust emission in the process of star formation. As YSOs are identified in the IC 443 region by infrared observations, further, high-resolution centimeter observations of that area would be of great importance for this study. Still, we note that any additional free–free component to our models (excluding a spinning dust component) is not favored. Of course, due to the low quality of currently known radio/microwave continuum of IC 443 we cannot draw any definite conclusions.

In their study of AME in Galactic clouds, Planck Collaboration Int. XV (2014) did not list the area of IC 443 as a candidate AME emission region (such as, e.g., the W48 region containing SNR W44). On the other hand, Planck Collaboration X et al. (2016) decomposed the full-mission all-sky *Planck* observations (Planck Collaboration I 2016) into several foreground components (i.e., synchrotron, free–free, AME, etc.), making use of both the nine-year *WMAP* data (Bennett et al. 2013) and the Haslam 408 MHz survey (Haslam et al. 1982). In that sense, among others, a full-sky map of the AME emission component was produced. Spanning the range from 408 MHz to 857 GHz in frequency, Planck Collaboration X (2016) actually performed foreground component separation within the framework of Bayesian `Commander` analysis (Eriksen et al. 2004, 2006, 2008). They

modeled the AME component as the sum of two spinning dust spectra with fixed spectral shape as determined by the SpDust code, but differing amplitudes and peak frequencies. In this phenomenological model, one of the spectra was required to have a spatially fixed peak frequency, fit to be 33.35 GHz, while the other peak frequency was allowed to vary freely from pixel to pixel. In that sense, it is worth checking the resulting AME foreground map from the *Planck* Legacy Archive[6] for any significant emission in the direction of the SNR IC 443. The AME map has an angular resolution of 1° FWHM with HEALPix[7] resolution of $N_{\rm side} = 256$ (Górski et al. 2005). Of course, one should bear in mind that the (mean and usually quoted) angular radius of the SNR is around 22′.5 (Green 2014).

Adopting the central radio coordinates of IC 443 from Green (2014), we measured counts in circular regions with radii 30′ and 1° for both AME components. Using the Rayleigh–Jeans formula we can roughly estimate the flux density from these regions (bearing in mind pixel dimensions of 21′ 21′). For component AME1 (with reference frequency of 22.8 GHz) this leads to around 6 Jy and 19 Jy, respectively. The results for component AME2 (with reference frequency of 41.0 GHz and spinning dust peak frequency of 33.35 GHz) are around 4 Jy and 11 Jy, for the analyzed circular regions, respectively. However, our model predictions for $S^{\rm Spd}$, from the analysis of the integrated radio to microwave continuum spectrum of IC 443, are a bit larger (even when we sum both AME components at the same frequency): 18 ± 6 Jy and 16 ± 4 Jy at 22.8 GHz, and 14 ± 8 Jy and 17 ± 7 Jy at 41.0 GHz, for models M1 and M2, respectively. In addition, due to the low resolution, these estimated values of AME Commander flux density do not represent only the emission from the SNR, but they also sample the emission from complex nearby regions (i.e., Galactic clouds that can be places of significant spinning dust emission; Planck Collaboration Int. XV 2014).

As noted by Planck Collaboration X (2016), although the Commander AME map provides a good tracer of spinning dust in our Galaxy, there are significant degeneracies between the free–free and AME components. That fact should be taken into consideration when using these foreground maps to estimate emissivities. There is also a possibility of significant leakage between synchrotron, AME (spinning dust), and free–free components. Such a leakage can generally be the source of a decrement in the Commander synchrotron maps (see, e.g., Planck Collaboration XXV 2016). We would like to emphasize that a very important drawback of the Commander fits is related to the particular synchrotron model. It is very simple and perhaps not even suitable for an SNR (see Planck Collaboration X 2016, and references therein for the definition of that model). Furthermore, the Commander synchrotron flux density at 408 MHz is around 92 Jy for the measured counts in a circular region of radius 30′ around the central position of IC 443. The estimates of flux density at the same frequency from our model fits are roughly around 225 Jy. At that particular continuum frequency the synchrotron component should dominate other proposed emission mechanisms for this SNR.

Bearing in mind the possibility of component separation as well as particular model-related issues, it is worth noting that the currently known AME foreground map at least does not rule out our hypothesis that spinning dust emission in the SNR IC 443 region can be significant enough to influence the currently known integrated radio/microwave continuum of this remnant.

In the end, it is worth mentioning that the LOFAR (Low-Frequency Array) allows detailed sensitive high-resolution studies of the low-frequency (10–240 MHz) radio sky (van Haarlem et al. 2013). With a possible baseline length of around a thousand kilometers, the angular resolution of LOFAR extends to sub-arcsecond scales. In that sense, it can be used to shed light on the physical origin of the low-frequency turnover in the integrated continuum radio spectrum of SNR IC 443. Complementary to the lowest radio frequencies, more data in the frequency range between 10 and 100 GHz, at much higher angular resolution than that of *Planck*, are needed to draw firm conclusions about the contribution of particular radiation mechanisms responsible for the observed shape of the integrated radio/microwave continuum of this remnant. ALMA (The Atacama Large Millimeter/Submillimeter Array), for example, will, upon completion, cover continuum frequencies in the range 31–950 GHz (ALMA Partnership et al. 2016). Depending on the particular configuration and frequency band, the angular resolution will range from several arcseconds to the order of milliarcseconds. In addition, observations by S-PASS (S-Band Polarization All Sky Survey) at 2.3 GHz and an angular resolution of around 9′, as well as observations by C-BASS (The C-Band All Sky Survey) at 5 GHz and QUIJOTE (Q-U-I JOint Tenerife CMB Experiment) at 10–40 GHz with rather poor angular resolution, of around 1°, will also help to considerably improve our knowledge of the continuum spectrum of several Galactic SNRs (Carretti 2011; Rubiño-Martín et al. 2012; King et al. 2014).

7. CONCLUSIONS

In this work, different emission models that can be responsible for the particular shape of the integrated radio/microwave continuum spectrum of Galactic supernova remnant IC 443 are tested and discussed.

1. Recent observations by the *Planck* space telescope make it possible to analyze the high-frequency part of radio/microwave emission from SNRs.
2. The possibility is emphasized that the slight bump in the integrated continuum of this remnant around 20–70 GHz is genuine and that it can be explained by the contribution from an additional emission mechanism such as spinning dust. In fact, even considering all the drawbacks of the presented analysis, the quality of the fit is significantly improved when spinning dust emission is included in the spectral model. In addition, the Commander AME foreground map does not rule out the possibility of significant spinning dust emission from the IC 443 region. Finally, models that include the high-frequency synchrotron bending of the IC 443 radio spectrum are favored.
3. New LOFAR data will presumably shed light on the physical origin of the low-frequency turnover in the integrated continuum radio spectrum of SNR IC 443. Complementary to the lowest radio frequencies, more data in the frequency range between 10 and 100 GHz, at much higher angular resolution than that of *Planck*, are needed to draw firm conclusions about the contribution of particular radiation mechanisms responsible for

[6] http://pla.esac.esa.int/pla
[7] http://healpix.sourceforge.net/

the observed shape of the integrated radio/microwave continuum of this remnant.

We would like to thank the anonymous referee for valuable suggestions that substantially improved this paper. In addition we would like to thank B. Arbutina and B. Vukotić for helpful comments. This work is a part of Project No. 176005 "Emission nebulae: structure and evolution" supported by the Ministry of Education, Science, and Technological Development of the Republic of Serbia. This work is also partially supported by a grant from the Natural Sciences and Engineering Research Council of Canada.

REFERENCES

Abdo, A. A., Ackermann, M., Ajello, M., et al. 2010, ApJ, 712, 459
Ackermann, M., Ajello, M., Allafort, A., et al. 2013, Sci, 339, 807
Ali-Haïmoud, Y. 2013, AdAst, 2013, 462697
Ali-Haïmoud, Y., Hirata, C., & Dickinson, C. 2009, MNRAS, 395, 1055
ALMA Partnership, Asayama, S., Biggs, A., de Gregorio, I., et al. 2016
AMI Consortium, Ainsworth, R. E., Scaife, A. M. M., Ray, T. P., et al. 2012, MNRAS, 423, 1089
AMI Consortium, Scaife, A. M. M., Green, D. A., Pooley, G. G., et al. 2010, MNRAS, 403, L46
Andrae, R., Schulze-Hartung, T., & Melchior, P. 2010, arXiv:1012.3754
Arbutina, B., Urošević, D., Andjelić, M. M., Pavlović, M. Z., & Vukotić, B. 2012, ApJ, 746, 79
Arbutina, B., Urošević, D., Vučetić, M. M., Pavlović, M. Z., & Vukotić, B. 2013, ApJ, 777, 31
Asaoka, I., & Aschenbach, B. 1994, A&A, 284, 573
Auchettl, K. A., Wong, B. T. T., Ng, C. Y., & Slane, P. O. 2016, HEAD Meeting, 15, 306.02
Baars, J. W. M., Genzel, R., Pauliny-Toth, I. I. K., & Witzel, A. 1977, A&A, 61, 99
Babu, G. J., & Feigelson, E. D. 1996, Astrostatistics (London: Chapman and Hall)
Beichman, C. A., Neugebauer, G., Habing, H. J., Clegg, P. E., & Chester, T. J. 1988, in Infrared Astronomical Satellite (IRAS) Catalogs and Atlases, Explanatory Supplement, 1
Bell, A. R. 1978, MNRAS, 182, 147
Bennett, A. S. 1962, MmRAS, 68, 163
Bennett, C. L., Bay, M., Halpern, M., et al. 2003, ApJ, 583, 1
Bennett, C. L., Larson, D., Weiland, J. L., et al. 2013, ApJS, 208, 20
Blain, A. W., Smail, I., Ivison, R. J., Kneib, J.-P., & Frayer, D. T. 2002, PhR, 369, 111
Blandford, R. D., & Ostriker, J. P. 1978, ApJL, 221, L29
Bocchino, F., & Bykov, A. M. 2001, A&A, 376, 248
Bozzetto, L. M., Filipović, M. D., Crawford, E. J., et al. 2010, SerAJ, 181, 43
Bozzetto, L. M., Filipović, M. D., Crawford, E. J., et al. 2012, RMxAA, 48, 41
Bozzetto, L. M., Filipović, M. D., Crawford, E. J., et al. 2013, MNRAS, 432, 2177
Braun, R., & Strom, R. G. 1986, A&A, 164, 193
Bridle, A. H., & Purton, C. R. 1968, AJ, 73, 717
Brogan, C. L., Lazio, T. J., Kassim, N. E., & Dyer, K. K. 2005, AJ, 130, 148
Bykov, A. M., Chevalier, R. A., Ellison, D. C., & Uvarov, Y. A. 2000, ApJ, 538, 203
Carretti, E. 2011, JApA, 32, 457
Castelletti, G., Dubner, G., Clarke, T., & Kassim, N. E. 2011, A&A, 534, 21
Chevalier, R. A. 1974, ApJ, 188, 501
Colla, G., Fanti, C., Fanti, R., et al. 1971, AJ, 76, 953
Cornett, R. H., Chin, G., & Knapp, G. R. 1977, A&A, 54, 889
Cruciani, A., Battistelli, E. S., Carretti, E., et al. 2016, MNRAS, 459, 4224
de Horta, A. Y., Filipović, M. D., Bozzetto, L. M., et al. 2012, A&A, 540, 25
Dickinson, C. 2013, AdAst, 2013, 162478
Draine, B. T., & Hensley, B. 2012, ApJ, 757, 103
Draine, B. T., & Lazarian, A. 1998a, ApJL, 494, L19
Draine, B. T., & Lazarian, A. 1998b, ApJ, 508, 157
Erickson, W. C. 1957, ApJ, 126, 480
Eriksen, H. K., Dickinson, C., Lawrence, C. R., et al. 2006, ApJ, 641, 665
Eriksen, H. K., Jewell, J. B., Dickinson, C., et al. 2008, ApJ, 676, 10
Eriksen, H. K., O'Dwyer, I. J., Jewell, J. B., et al. 2004, ApJS, 155, 227
Fesen, R. A. 1984, ApJ, 281, 658
Gaensler, B. M., Chatterjee, S., Slane, P. O., et al. 2006, ApJ, 648, 1037
Gao, X. Y., Han, J. L., Reich, W., et al. 2011, A&A, 529, 159
Génova-Santos, R., Rubiño-Martín, J. A., & Peláez-Santos, A. 2017, MNRAS, 464, 4107
Górski, K. M., Hivon, E., Banday, A. J., et al. 2005, ApJ, 622, 759
Green, D. A. 2014, A Catalogue of Galactic Supernova Remnants (2014 May version) (Cambridge: Cavendish Laboratory) (available at "http://www.mrao.cam.ac.uk/surveys/snrs/")
Haslam, C. G. T., Salter, C. J., Stoffel, H., & Wilson, W. E. 1982, A&AS, 47, 1
Heiles, C. 1984, ApJS, 55, 585
Hensley, B., Murphy, E., & Staguhn, J. 2015, MNRAS, 449, 809
Hensley, B. S., Draine, B. T., & Meisner, A. M. 2016, ApJ, 827, 45
Hewitt, J. W., Grondin, M.-H., Lemoine-Goumard, M., et al. 2012, ApJ, 759, 89
Hezareh, T., Wiesemeyer, H., Houde, M., Gusdorf, A., & Siringo, G. 2013, A&A, 558, 45
Hoang, T., Draine, B. T., & Lazarian, A. 2010, ApJ, 715, 1462
Hoang, T., & Lazarian, A. 2016, ApJ, 821, 91
Hoang, T., Lazarian, A., & Draine, B. T. 2011, ApJ, 741, 87
Hoffman, I. M., Goss, W. M., Brogan, C. L., Claussen, M. J., & Richards, A. M. S. 2003, ApJ, 583, 272
Houde, M., Hezareh, T., Jones, S., & Rajabi, F. 2013, ApJ, 764, 24
Howard, W. E., III, & Dickel, H. R. 1963, PASP, 75, 149
Humphreys, R. M. 1978, ApJS, 38, 309
Irfan, M. O., Dickinson, C., Davies, R. D., et al. 2015, MNRAS, 448, 3572
Kawasaki, M. T., Ozaki, M., Nagase, F., et al. 2002, ApJ, 572, 897
Kilpatrick, C. D., Bieging, J. H., & Rieke, G. H. 2016, ApJ, 816, 1
King, O. G., Jones, M. E., Blackhurst, E. J., et al. 2014, MNRAS, 438, 2426
Kokusho, T., Nagayama, T., Kaneda, H., et al. 2013a, ApJL, 768, L8
Kokusho, T., Nagayama, T., Kaneda, H., et al. 2013b, in Proc. Life Cycle of Dust in the Universe: Observations Theory, and Laboratory Experiments, Proc. Science, ed. A. Andersen et al., 86
Koo, B.-C., Heiles, C., Stanimirović, S., & Troland, T. 2010, AJ, 140, 262
Kundu, M. R., & Velusamy, T. 1972, A&A, 20, 237
Leahy, D. A. 2004, AJ, 127, 2277
Leahy, D. A., & Roger, R. S. 1998, ApJ, 505, 784
Lee, J.-J., Koo, B.-C., Yun, M. S., et al. 2008, AJ, 135, 796
Mandolesi, N., Bersanelli, M., Butler, R. C., et al. 2010, A&A, 520, 3
Markwardt, C. B. 2009, in ASP. Conf. Ser. 411, Astronomical Data Analysis Software and Systems XVIII, ed. D. A. Bohlender, D. Durand, & P. Dowler (San Francisco, CA: ASP), 251
Miceli, M., Bocchino, F., Decourchelle, A., et al. 2013, A&A, 556, 80
Miceli, M., Bocchino, F., Decourchelle, A., et al. 2014, AN, 335, 252
Ohnishi, T., Uchida, H., Tsuru, T. G., et al. 2014, ApJ, 784, 74
Olbert, C. M., Clearfield, C. R., Williams, N. E., Keohane, J. W., & Frail, D. A. 2001, ApJL, 554, L205
Oliva, E., Lutz, D., Drapatz, S., & Moorwood, A. F. M. 1999, A&A, 341, L75
Onić, D. 2015, SerAJ, 191, 29
Onić, D., & Urošević, D. 2015, ApJ, 805, 119
Onić, D., Urošević, D., Arbutina, B., & Leahy, D. 2012, ApJ, 756, 61
Ostrowski, M. 1999, A&A, 345, 256
Petre, R., Szymkowiak, A. E., Seward, F. D., & Willingale, R. 1988, ApJ, 335, 215
Pivato, G., Hewitt, J. W., Tibaldo, L., et al. 2013, ApJ, 779, 179
Planck Collaboration I (Planck 2015 results), Adam, R., Ade, P. A. R., Aghanim, N., et al. 2016, A&A, 594, 1
Planck Collaboration VI (Planck 2015 results), Ade, P. A. R., Aghanim, N., Ashdown, M., et al. 2016, A&A, 594, 6
Planck Collaboration VIII (Planck 2015 results), Adam, R., Ade, P. A. R., Aghanim, N., et al. 2016, A&A, 594, 8
Planck Collaboration X (Planck 2015 results), Adam, R., Ade, P. A. R., Aghanim, N., et al. 2016, A&A, 594, 10
Planck Collaboration XI (Planck 2013 results), Abergel, A., Ade, P. A. R., Aghanim, N., et al. 2014, A&A, 571, 11
Planck Collaboration Int. XV (Planck intermediate results), Ade, P. A. R., Aghanim, N., Alves, M. I. R., et al. 2014, A&A, 565, 103
Planck Collaboration XXI (Planck early results), Abergel, A., Ade, P. A. R., Aghanim, N., et al. 2011, A&A, 536, 21
Planck Collaboration XXV (Planck 2015 results), Ade, P. A. R., Aghanim, N., Alves, M. I. R., et al. 2016, A&A, 594, 25
Planck Collaboration Int. XXXI (Planck intermediate results), Arnaud, M., Ashdown, M., Atrio-Barandela, F., et al. 2016, A&A, 586, 134
Planck HFI Core Team VI, Ade, P. A. R., Aghanim, N., et al. 2011, A&A, 536, A6
Pohl, M., Wilhelm, A., & Telezhinsky, I. 2015, A&A, 574, 43
Reich, W., Zhang, X., & Fürst, E. 2003, A&A, 408, 961

Reynolds, S. P. 1998, ApJ, 493, 375
Reynolds, S. P. 2008, ARA&A, 46, 89
Reynolds, S. P. 2009, ApJ, 703, 662
Reynolds, S. P., & Ellison, D. C. 1992, ApJL, 399, L75
Rho, J., Jarrett, T. H., Cutri, R. M., & Reach, W. T. 2001, ApJ, 574, 885
Rho, J., & Petre, R. 1998, ApJ, 503, 167
Rubiño-Martín, J. A., Rebolo, R., Aguiar, M., et al. 2012, Proc. SPIE, 8444, 84442Y
Saken, J. M., Fesen, R. A., & Shull, J. M. 1992, ApJS, 81, 715
Scaife, A. 2012, AstRv, 7, 26
Scaife, A., Green, D. A., Battye, R. A., et al. 2007, MNRAS, 377, L69
Shinn, J.-H., Koo, B.-C., Seon, K.-I., & Lee, H.-G. 2011, ApJ, 732, 124
Silsbee, K., Ali-Haïmoud, Y., & Hirata, C. 2011, MNRAS, 411, 2750
Stevenson, M. A. 2014, ApJ, 781, 113
Su, Y., Fang, M., Yang, J., Zhou, P., & Chen, Y. 2014, ApJ, 788, 122
Swartz, D. A., Pavlov, G. G., Clarke, T., et al. 2015, ApJ, 808, 84
Tang, X., & Chevalier, R. A. 2014, ApJL, 784, L35
Tang, X., & Chevalier, R. A. 2015, ApJ, 800, 103
Tavani, M., Giuliani, A., Chen, A. W., et al. 2010, ApJ, 710, 151
Tibbs, C. T., Paladini, R., Cleary, K., et al. 2015, MNRAS, 453, 3356
Troja, E., Bocchino, F., Miceli, M., & Reale, F. 2008, A&A, 485, 777
Uchiyama, Y., Blandford, R. D., Funk, S., Tajima, H., & Tanaka, T. 2010, ApJ, 723, 122
Urošević, D. 2014, Ap&SS, 354, 541
van der Laan, H. 1962, MNRAS, 124, 125
van Haarlem, M. P., Wise, M. W., Gunst, A. W., et al. 2013, A&A, 556, 2
Vink, J. 2012, A&ARv, 20, 49
Weiland, J. L., Odegard, N., Hill, R. S., et al. 2011, ApJS, 192, 19
Welsh, B. Y., & Sallmen, S. 2003, A&A, 408, 545
Wood, D. O. S., & Churchwell, E. 1989, ApJS, 69, 831
Xiao, L., Fürst, E., Reich, W., & Han, J. L. 2008, A&A, 482, 783
Yamaguchi, H., Ozawa, M., Koyama, K., et al. 2009, ApJL, 705, L6
Ysard, N., Juvela, M., & Verstraete, L. 2011, A&A, 535, 89
Ysard, N., Miville-Deschênes, M. A., & Verstraete, L. 2010, A&A, 509, 1
Ysard, N., & Verstraete, L. 2010, A&A, 509, 12
Zirakashvili, V. N., & Aharonian, F. 2007, A&A, 465, 695